

# JOINT INVERSION OF PRESSURE AND TIME-LAPSE ELECTROMAGNETIC LOGGING MEASUREMENTS

F.O. Alpak<sup>1</sup>, T.M. Habashy<sup>2</sup>, C. Torres-Verdín<sup>1</sup>, and E.B. Dussan V.<sup>2</sup>

<sup>1</sup>*The University of Texas at Austin*

<sup>2</sup>*Schlumberger-Doll Research*

## ABSTRACT

We develop a novel algorithm for the integrated petrophysical evaluation of hydrocarbon-bearing formations using dual-physics measurement data. Specific data sets used in this paper are (a) time-lapse electromagnetic (EM) measurements acquired with an array induction logging tool, and (b) pressure measurements acquired with a multi-probe wireline formation tester in a vertical borehole. Dynamic behavior of saturation and salt concentration distributions due to mud-filtrate invasion creates a two-phase three-component flow system. In this work, the inverse problem associated with dual-physics wireline measurements consists of the estimation of a two-dimensional (2D) axisymmetric petrophysical model described by layered parametric spatial distribution of both vertical and horizontal absolute permeabilities and porosities.

We pose the inverse problem of estimating layer petrophysical parameters from discrete time-lapse EM induction and pressure measurements as an optimization problem. A weighted least-squares constrained optimization method is employed to solve the inverse problem. Tool responses within the framework of the iterative inversion scheme are numerically computed via simulating dynamic physics of two-phase three-component flow that takes place during mud-filtrate invasion and subsequent formation testing. Time-lapse EM induction measurements are simulated in a coupled mode to the fluid flow.

Numerical examples have shown that the benefit of the joint inversion algorithm described in this paper is in the reduction of the nonuniqueness associated with the estimation process by simultaneously honoring two sets of complementary measurements that contain independent information about the underlying model.

## INTRODUCTION

Robust and accurate determination of fluid-flow related petrophysical parameters from

borehole measurements is one of the fundamental problems of quantitative well log interpretation. Introduction of the concepts of fluid flow to the analysis of geoelectrical log measurements improves the physical consistency of the interpretation. In addition, log measurements can be jointly interpreted with fluid-flow related measurements to reduce nonuniqueness in the quantitative estimation of petrophysical parameters.

Physics of multi-phase fluid-flow and EM induction phenomena in porous media can be coupled by means of an appropriate saturation equation. Thus, a dual-physics stencil for the quantitative joint interpretation of geoelectrical and flow-related measurements can be formulated to yield a rigorous estimation of the underlying petrophysical model. Dynamic characteristics of mud-filtrate invasion phenomenon form the basis for quantitative petrophysical interpretation of conductivity profiles around the borehole by employing two-phase fluid-flow physics and geoelectrical modeling. Tobola, Yao, and Holditch (1991, 1996) reported successful employment of time-lapse induction log responses to estimate reservoir absolute permeability by means of a history matching method for fresh mud-filtrate invaded into low permeability gas reservoirs. Semmelbeck *et al.* (1995) also attempted to estimate absolute permeability for low permeability gas sands from array logs. Ramakrishnan and Wilkinson (1997, 1999) developed a method for the inversion of fractional flow curve from conductivity profiles around the borehole by using fluid-flow physics. They also applied this approach to predict production water cuts as a function of depth in the wellbore. Recently, Zeybek *et al.* (2001) made use of pressure and flowline water-cut data from dual-packer formation tester interval tests, and openhole array resistivity measurements to estimate saturation-dependent two-phase relative permeabilities. Here, a numerical reservoir simulator was used to simulate two-phase flow during sampling. Epov *et al.* (2002) performed inversions of high-frequency EM logging

measurements to yield resistivity and salt concentration profiles consistent with two-phase hydrodynamic analysis of mud-filtrate invasion.

Inspired by the aforementioned dual-physics efforts, the objective of the work reported in this paper is to develop a robust, accurate, and efficient algorithm for the parametric joint inversion of EM induction and formation pressure measurements. The inversion algorithm will yield petrophysical properties, namely, layer-by-layer horizontal and vertical absolute permeabilities, and porosities of the hydrocarbon-bearing formations. Inversion of dual-physics measurements is posed as an optimization problem where a quadratic objective function is minimized subject to physical constraints on the model. A modification of the gradient-based iterative Gauss-Newton optimization technique is utilized for the inversions (Habashy, 2003). At each iterative step, the solution of the forward problem is required. Forward modeling of dual-physics measurements entails coupled simulations of mud-filtrate invasion, wireline formation test measurements, and induction logging measurements. We utilize efficient three-dimensional finite-difference algorithms to simulate multi-phase fluid-flow and EM induction phenomena (Aziz and Settari, 1979; Druskin *et al.*, 1999). Pressure, saturation, and salt concentration fields generated during water-base mud-filtrate invasion, and a subsequent wireline formation test are modeled as two-phase convective transport of three components, namely, oil/gas, water, and salt. Coupling between two-phase flow and EM induction physics is accomplished via Archie's saturation equation. Isothermal salt mixing phenomenon taking place within the aqueous-phase due to the invading and in-situ salt concentration contrast is also taken into account by means of a brine conductivity model (Zhang *et al.*, 1999).

Proof-of-concept examples of the joint inversion method are successfully conducted for single-well 2D axisymmetric models that involve noisy and noise-free synthetically generated EM induction and pressure measurements. In one of these examples, we carry out joint as well as independent inversions of induction logging and dual-packer formation tester measurements for the purpose of comparison. For all of the investigated cases, the effect of mud-filtrate invasion is rigorously taken into account by making use of a novel numerical algorithm that simulates the physics of mud-filtrate invasion. The reported work confirms that the intrinsic value of each piece of

data considerably improves when used in a cooperative, integrated fashion, and under a common petrophysical model. Consequently, measurement types that are considered to be of low vertical resolution but of large depth of investigation (i.e., pressure measurements) can be efficiently integrated with measurements that exhibit a relatively shallow depth of investigation but higher vertical resolution (i.e., induction measurements) into a common petrophysical model.

### COMPUTATION OF MUD-FILTRATE INVASION RATE

In this paper, we use a general numerical algorithm designed to simulate the physics of mud-filtrate invasion in vertical and highly deviated boreholes. This numerical scheme is adapted by Wu *et al.* (2002) from an existing multi-phase fluid-flow simulator developed by The University of Texas at Austin, and commercially referred to as UTCHEM (Delshad *et al.*, 1996).

Numerical modeling of mud-filtrate invasion via UTCHEM yields an equivalent time-domain filtrate flow rate function. Given the pressure overbalance condition, invasion geometry, and mudcake properties, this function replicates time-dependent behavior of the mudcake. Due to the fact that clay platelets form a mudcake with permeabilities in the order of  $10^{-3}$  mD, the filtrate invasion rate is predominantly controlled by the mudcake, with minimal influence of the formation permeability (Ramakrishnan and Wilkinson, 1997). Extensive simulations conducted with UTCHEM are in agreement with the above observation. In turn, a numerically computed invasion rate schedule can be imposed as a local source condition (flux as a function of depth) to an effective fluid-flow simulator. As such, the physics of mud-filtrate invasion can be incorporated into a coupled algorithm for the simulation of multi-phase fluid-flow and EM induction phenomena.

### FORMULATION OF THE FORWARD MODEL FOR DUAL-PHYSICS MEASUREMENTS

Invasion of water-base mud-filtrate into a partially saturated hydrocarbon-bearing porous medium and a subsequent multi-probe dual-packer formation test involve two-phase multi-component fluid transport. Time- and space-domain distributions of water saturation, salt concentration, and pressure are modeled as convective transport of hydrocarbon and aqueous phases, and hydrocarbon, water, and salt components. Ions

present in the system are assumed to be soluble only within the aqueous phase and lumped into a single salt component. In the formulation of the forward problem, we assume the existence of a salt concentration contrast between the in-situ formation brine and the invading mud-filtrate. According to Ramakrishnan and Wilkinson (1997) diffusion has only a small effect at invasion radius length scales. In addition, equilibration of salt concentration among pores occurs at time scales smaller than the invasion time scale, whereupon local level aqueous phase salt concentrations remain the same from pore to pore. Therefore, for the problem of interest, we only consider convective miscible transport of the salt component within the aqueous phase and neglect diffusional spreading of the interface between mud-filtrate and formation brine.

Simulation of isothermal two-phase flow in a partially saturated hydrocarbon-bearing medium requires of mass balance and transport equations as well as a constitutive equation of state. We disregard the presence of chemical reactions, rock/fluid mass transfer, and diffusive/dispersive transport. The mass balance equation for the  $i^{\text{th}}$  fluid phase can be stated as follows (Aziz and Settari, 1979)

$$\frac{\partial(\mathbf{r}_i \mathbf{f} S_i)}{\partial t} + \nabla \cdot (\mathbf{r}_i \mathbf{?}_i) = -q_{vi}, \quad i = 1, 2. \quad (1)$$

We model flow in the near-borehole region of a single vertical well intersecting a hydrocarbon-bearing horizontal reservoir in  $R^3$ . Consistent with the flow geometry imposed by the wireline formation tester, a cylindrical coordinate system is employed to accurately represent the dynamics of reservoir behavior in the spatial domain of interest. Spatial support for material balance equations is then  $\Omega = \{(r, \mathbf{q}, z) \in R^3 : r_w \leq r \leq r_e, 0 \leq \mathbf{q} \leq 2\pi, 0 \leq z \leq h\}$ . In equation (1),  $\mathbf{r}$ ,  $\mathbf{?}$ ,  $\mathbf{f}$ ,  $q_v$ , and  $S$  denote fluid density, fluid velocity vector, porosity, source/sink term, and phase saturation, respectively. The subscript  $i$  designates the phase index. Moreover,  $r_w$ ,  $r_e$ , and  $h$  stand for borehole radius, external radius of the formation, and total formation thickness, respectively. No-flow boundary conditions are imposed on the upper, lower, and outer limits of the formation. The external boundary of the formation is located relatively far away from the wellbore. A constant rate internal boundary condition is imposed to the borehole wall time-step-by-time-step. In this fashion, time-

variant invasion rate history and other formation test related rate schedules are incorporated into our simulations in a time-stepwise discrete fashion. In our formulation, Darcy's law is the governing transport equation, i.e.,

$$\mathbf{?}_i = -\bar{\mathbf{k}} \cdot \frac{k_{ri}}{\mathbf{m}_i} (\nabla p_i - \mathbf{g}_i \nabla D_z), \quad (2)$$

where  $\bar{\mathbf{k}}$  is the absolute permeability tensor of the porous medium,  $k_r$  is the relative permeability,  $\mathbf{m}$  is the phase viscosity,  $p$  is the phase pressure,  $\mathbf{g}$  is the phase specific gravity, and  $D_z$  is the vertical location below some reference level. Finally, the constituent equation follows from the equation of state. The assumption is also made that both fluid and rock compressibilities are constant over the pressure range of interest for the simulations that involve simultaneously flowing oleic and aqueous phases, and are given by

$$c_{fl} = -\frac{1}{V} \frac{\partial V}{\partial p} \Big|_T = \frac{1}{\mathbf{r}} \frac{\partial \mathbf{r}}{\partial p} \Big|_T, \quad (3)$$

and

$$c_r = \frac{1}{\mathbf{f}} \frac{\partial \mathbf{f}}{\partial p} \Big|_T. \quad (4)$$

The above assumption of constant fluid compressibility does not hold for the two-phase flow of gaseous and aqueous phases. Thus, in this case, gas compressibility is treated as a function of the pressure-volume-temperature properties of gas for each time-step. Capillary pressures and fluid saturations are governed by

$$P_c = p_{nw} - p_w, \quad (5)$$

and

$$S_{nw} + S_w = 1.0, \quad (6)$$

where the subscripts  $nw$  and  $w$  stand for nonwetting and wetting phases.

Convective transport of the salt component is simulated after a converged solution for the time-step has been found, and the interblock flows are determined. A mass conservation equation is solved to update the spatial distribution of salt concentrations,  $C_w$ , and is given by

$$\frac{\partial(\mathbf{r}_w \mathbf{f} S_w C_w)}{\partial t} + \nabla \cdot (\mathbf{r}_w \mathbf{?}_w S_w C_w) = -C_{wi} q_i. \quad (7)$$

In equation (7),  $C_{wi}$  and  $q_i$  stand for the concentration of invading mud-filtrate, and invasion rate at a given time-step, respectively.

Numerical modeling of the described two-phase, three-component fluid-flow problem in a permeable formation is accomplished using a finite-difference based reservoir simulator, namely, ECLIPSE<sup>TM</sup> <sup>(§)</sup> in fully implicit, black-oil mode. Time- and space-domain distributions of water saturation, salt concentration, and pressure due to mud-filtrate invasion and a subsequent formation tester drawdown-build-up sequence are simulated with ECLIPSE<sup>TM</sup>.

Spatial distributions of aqueous phase saturation corresponding to each logging time are subsequently transformed into snapshots of electrical conductivity using Archie's law,

$$\mathbf{s} = (1/a) \mathbf{s}_w \mathbf{f}^m \mathbf{S}_w^n, \quad (8)$$

(Archie, 1942) applied grid-by-grid. In the above equation,  $\mathbf{s}$ ,  $\mathbf{s}_w$ , and  $\mathbf{S}_w$  denote formation conductivity, brine conductivity, and aqueous phase saturation, respectively. Porosity and saturation exponents  $m$  and  $n$ , and normalization parameter  $a$  are empirical constants.

Spatial distributions of brine conductivity at each logging time are computed grid-by-grid using the following transformation from simulated salt concentrations (Zhang *et al.*, 1999)

$$\mathbf{s}_w = \left[ \left( 0.0123 + \frac{3647.5}{C_w^{0.955}} \right) \frac{82}{1.8T + 39} \right]^{-1}, \quad (9)$$

where,  $C_w$  and  $T$  stand for salt concentration in [ppm] and formation temperature in [ $^{\circ}$ C], respectively. As such, the dependency of grid block conductivity on the aqueous phase salt concentration is taken into account. The main assumption underlying the brine conductivity model is the instantaneous temperature equilibrium between invading and in-situ aqueous phases.

Forward modeling of array induction logging sonde responses requires the solution of the following frequency-domain problem for Maxwell's equations:

$$\nabla \times \mathbf{E} + i\omega \mathbf{m} \mathbf{H} = 0, \quad (10a)$$

$$\nabla \times \mathbf{H} - \mathbf{s} \mathbf{E} = -\mathbf{J}. \quad (10b)$$

Here,  $\mathbf{E}$  is the electric field vector,  $\mathbf{H}$  is the magnetic field vector, and  $\mathbf{J}$  is the external electric current source vector. The symbols  $\mathbf{s} = \mathbf{s}(x, y, z)$

and  $\mathbf{m}$  denote the conductivity coefficient and the magnetic permeability, respectively. Consistent with the nature of low frequency EM induction applications, the displacement current is assumed to be negligible. Equations (10a) and (10b) can be combined into the following equation for electric field  $\mathbf{E}$ ,

$$\mathbf{s}^{-1} \nabla \times \nabla \times \mathbf{E} + i\omega \mathbf{s} \mathbf{E} = i\omega \mathbf{s}^{-1} \mathbf{J}. \quad (11)$$

For the numerical solution of equation (11), a finite-difference algorithm SLDMINV (Druskin *et al.*, 1999) on a set of staggered grid is employed using a Spectral Lanczos Decomposition Method that computes inverse powers of the stiffness matrix to yield efficient multi-frequency simulations of induction tool responses in terms of magnetic field computations. Spatial distributions of conductivity,  $\mathbf{s}$ , are computed from fluid-flow simulation results for aqueous phase saturations and salt concentrations at each logging time. Conductivities computed from flow simulations on the 3D cylindrical grid are mapped to the 3D Cartesian grid of SLDMINV by means of a robust material-averaging stencil (Moscow *et al.*, 1999). The corresponding array induction logging tool responses are simulated by means of SLDMINV for each snapshot in time.

#### THE INVERSE PROBLEM AND THE INVERSION ALGORITHM

In the inverse problem, time-lapse measurements of the vertical component of total magnetic field,  $H_z$ , is conducted at multiple receiver locations, frequencies, and at various logging times with a depth-profiling sonde [see, for example, Fig. 1(a)]. In addition, we consider the availability of multi-probe pressure transient measurements,  $p(t)$ , acquired by a wireline formation tester shown in Fig. 1(b). As formulated in the previous section, the forward model for coupled dual-physics measurements is a nonlinear function of the spatial distribution of absolute permeabilities and porosities and other relevant rock and fluid properties. We assume the availability of other rock and fluid properties from various logs and laboratory experiments. The objective of our work is the joint inversion of layer-by-layer horizontal and vertical absolute permeabilities and porosities from time-lapse EM induction and pressure transient measurements.

Joint inversion of the underlying petrophysical model is posed as an optimization problem that involves the minimization of an objective function

<sup>(§)</sup> Mark of Schlumberger

subject to physical constraints (Habashy, 2003). We adopt the following objective function,  $C(\mathbf{x})$ , (Torres-Verdín and Habashy, 1994)

$$C(\mathbf{x}) = \frac{1}{2} \left[ \mathbf{m} \left\{ \|\mathbf{W}_d \cdot \mathbf{e}(\mathbf{x})\|^2 - c^2 \right\} + \|\mathbf{W}_x \cdot (\mathbf{x} - \mathbf{x}_p)\|^2 \right]. \quad (12)$$

In the above expression, we define the vector of residuals,  $\mathbf{e}(\mathbf{x})$ , as a vector whose  $j^{\text{th}}$  element is the residual error (data mismatch) of the  $j^{\text{th}}$  measurement. We define the residual error as the difference between the measured and predicted normalized responses, given by

$$\mathbf{e}(\mathbf{x}) = [(S_1(\mathbf{x}) - m_1), \dots, (S_M(\mathbf{x}) - m_M)]^T = \mathbf{S}(\mathbf{x}) - \mathbf{m}. \quad (13)$$

In the above expression,  $M$  is the number of measurements,  $m_j$  denotes the normalized observed response (measured data), and  $S_j$  corresponds to the normalized simulated response as predicted by the vector of model parameters,  $\mathbf{x}$ , given by

$$\mathbf{x} = [x_1, \dots, x_N]^T = \mathbf{y} - \mathbf{y}_R, \quad (14)$$

where  $N$  is the number of unknowns. The vector of model parameters,  $\mathbf{x}$  is represented as the difference between the vector of the actual model parameters,  $\mathbf{y}$ , and a reference model,  $\mathbf{y}_R$ . All *a-priori* information on the model parameters such as those derived from independent measurements are provided by the reference model. The scalar factor  $\mathbf{m}$ , i.e.,  $(0 < \mathbf{m} < \infty)$  is a regularization parameter (also called a Lagrange multiplier) for determining the relative importance of the two terms of the objective function. The choice of  $\mathbf{m}$  produces an estimate of the model  $\mathbf{x}$  that has a finite minimum weighted norm away from a prescribed model,  $\mathbf{x}_p$ , and which globally misfits the data. The second term in the objective function is included to regularize the optimization problem. This term suppresses any possible magnification of errors in the parameter estimation due to measurement noise. The matrix  $\mathbf{W}_x \mathbf{W}_x^T$  is the inverse of the model covariance matrix that represents the degree of confidence in the prescribed model,  $\mathbf{x}_p$ , and  $\mathbf{W}_d^T \mathbf{W}_d$  is the inverse of the data covariance matrix describing the estimated uncertainties in the data, i.e., due to noise contamination. We employ the following form of

the vector residual with the purpose of putting the various measurements on equal footings,

$$\|\mathbf{W}_d \cdot \mathbf{e}(\mathbf{x})\|^2 = \sum_{j=1}^M w_j \left| \frac{S_j(\mathbf{x})}{m_j} - 1 \right|^2. \quad (15)$$

In our inversion algorithm the vector of measurements,  $\mathbf{m}$ , is constructed with two categories of data: (a) multi-probe formation tester pressure-rate measurements as a function of time, and (b) multi-receiver, multi-frequency, and multi-snapshot (time-lapse) EM induction measurements acquired by a depth-profiling sonde. If desired, the described algorithm can also be used for single-data-type inversions.

In this work, we focus only on vertical variability in the petrophysical model. Horizontal geological layers of various thicknesses characterize the reservoir geometry. The vector of model parameters,  $\mathbf{x}$ , is made up of the layer-by-layer parametric spatial distribution of horizontal and vertical absolute permeabilities, and porosities. A schematic of the model domain parameterization is shown in Fig. 2. Here, we assume the availability of information about the locations of layer boundaries from other types of logs such as borehole images. Based on the extent of the available measurement data and *a-priori* information, an arbitrary combination of the above mentioned petrophysical parameters can be included in  $\mathbf{x}$ .

To solve the nonlinear inverse problem, we employ a modification of the Gauss-Newton method. The inverted model parameters,  $\mathbf{x}$ , are constrained to be within their physical bounds using a nonlinear transformation (Habashy, 2003). Such a nonlinear transformation maps a constrained minimization problem into an unconstrained one. A backtracking line search algorithm is used along the descent direction to guarantee a reduction of the objective function from one iteration step to the next. The choice of the Lagrange multiplier is adaptively linked to the condition number of the Hessian matrix of the Gauss-Newton method. The weight of the misfit term in the objective function is progressively increased with respect to the regularization term as the inversion algorithm iterates towards the optimum and nonuniqueness in the inversion reduces. In this fashion, the stability property of the solution obtained at each iteration level is enhanced without overbiasing the final solution to the stabilizing regularization term. Evaluation of the

Hessian matrix is the most computationally intensive part of the inversion. Four alternative approximate update methods for the Hessian matrix which eliminate expensive computations are employed to accelerate the inversions. Explored approximation schemes are: Broyden symmetric rank-one, Powell-Symmetric-Broyden (PSB) rank-two, Davidson-Fletcher-Powell (DFP) rank-two, and Broyden-Fletcher-Goldfarb-Shanno (BFGS) rank-two update methods (Gill *et al.*, 1981).

### NUMERICAL EXAMPLES

A vertical borehole is considered to intersect a hydrocarbon-bearing horizontal formation comprising of a single thick-layer in our first test case. In addition to the permeable layer, sealing upper and lower shoulder beds are included in the geoelectrical model [see Fig. 3(a)]. From the onset of drilling, the permeable formation is subject to dynamic water-base mud-filtrate invasion. At the first logging time, an array induction log is recorded across the formation. The tool assumed for EM induction measurements is the Array Induction Imager Tool, AIT™<sup>(\*)</sup>, described schematically in Fig. 1(a). This sonde is used to ensure the availability of data with multiple depths of investigation (Hunka *et al.*, 1990). The second available data type is multi-probe formation pressure transient measurements acquired with the Modular Formation Dynamics Tester, MDT™<sup>(+)</sup>. A dual-packer/probe module configuration with two vertical observation probes is considered as the measurement platform (Pop *et al.*, 1993; Ayan *et al.*, 2001). Figure 1(b) shows a schematic of the packer and probe modules. Soon after the first induction log is recorded, the multi-probe formation tester configuration is deployed across the formation of interest to conduct pressure transient measurements. Time-series of pressure responses are recorded at two observation probe locations, and at the center of the dual-packer open interval in response to a controlled flow rate pulse. A post transient-test EM induction log senses the perturbed two-phase flow field caused by the formation tester experiment. This measurement schedule involves acquisition of dual-physics data and, is here referred to as log-test-log strategy.

Given favorable flow conditions and sufficient test duration, pressure transient measurements conducted by the dual-packer and tandem observation probes contain significant information about horizontal and vertical permeabilities ( $k_h$  and  $k_v$ ), when reliable *a-priori* information about

the group  $fC_t$  is available (Ayan *et al.*, 2001). Here, we assume the availability of laboratory measurements of fluid properties that determine the total compressibility,  $C_t$ , or its dependence on pressure. Additionally, in our forward model, movement of saturations and salt concentrations due to convective transport of fluids is robustly linked to spatial distributions of conductivity via a saturation equation. Thus, provided that the choice of saturation equation is appropriate for the formation of interest, information about porosity,  $f$ , can be robustly extracted from time-lapse EM measurements within the framework of the joint inversion scheme.

With the purpose of establishing a basis of comparison for the joint inversion approach, we also considered the inversion of time-lapse EM data alone for the zeroth order homogeneous and isotropic single-layer formation model. This schedule involves acquisition of two induction logs performed at two separate times. The formation is subject to mud-filtrate invasion during the time gaps between drilling, the first log, and the second log. This schedule is referred to as time-lapse log strategy.

Formation rock and fluid properties, specific instrumental details, and scheduling of the above described measurement strategies are listed in Table 1. We used a  $31 \times 6 \times 30$  grid in the cylindrical coordinate system as the result of extensive finite-difference gridding studies to produce computationally efficient, internally consistent, and accurate numerical simulations. This grid is uniform in the vertical and azimuthal directions. Block sizes increase logarithmically in the radial direction away from the borehole. A vertical cross-section of this grid is shown in Fig. 4. Capillary pressure effects are assumed to be negligible. The relative permeability function used for this case is illustrated in Fig. 5(a).

The following schedule is assumed for log-test-log strategy. The first induction log is recorded at the 3<sup>rd</sup> day of mud-filtrate invasion. A subsequent wireline formation test is scheduled to last 300 min. During the formation test, fluid is withdrawn from the formation at a constant liquid rate of 30 rbb/d for 100 min and the formation pressure drawdown response is observed across the dual-packer interval and at the observation probes. Subsequently, the tool is shut down for another 200 min and the formation pressure build-up response is recorded. In the example cases, we only consider the use of pressure data sampled during the build-

(\*), (+) Mark of Schlumberger

up period of the formation test. Upon conclusion of the formation test, the second induction log is recorded. For the time-lapse log strategy, the first induction log is also recorded at the 3<sup>rd</sup> day of invasion. Yet, the formation is subjected to mud-filtrate invasion for a week before the second induction log is recorded at the 10<sup>th</sup> day.

For Case 1, simulated mud-filtrate invasion history until the first logging time is shown in Fig. 6(a). Rate history is rendered into a two-step rate schedule via integral averaging of the early time-transient into an early-time equi-volume step-rate. For the time-lapse logging strategy, the invasion rate schedule is extended further until the second logging time. As shown in Fig. 6(b), the rate domain response of the removal of mudcake due to drill-string trip-out at the first logging time is also incorporated into the mud-filtrate invasion history.

Joint inversions of time-lapse magnetic field and pressure measurements (log-test-log schedule) and inversions of time-lapse magnetic field measurements (time-lapse log schedule) are performed to yield isotropic formation absolute permeability,  $k$ , and porosity,  $f$ . True and initial guess values are  $k = 100$  mD,  $f = 0.25$ , and  $k = 40$  mD,  $f = 0.12$ , respectively. The effect of noise on the inversion results is assessed by adding zero-mean Gaussian random (white) noise to the synthetically-generated measurements. Inversion results are reported in Table 2 along with the number of Gauss-Newton iterations required to achieve convergence. Joint inversion of dual-physics data is performed using two data weighting strategies for each noise level. In the first strategy, both EM and pressure data are weighted uniformly. In the second strategy, weight coefficients of EM data are made equal to three times of those used for pressure data. In this case, the inversion is clearly biased to fit the EM data. At low noise levels, all measurement and inversion strategies yield accurate estimations. In comparison to other approaches, the uniform-weight joint inversion strategy consistently requires fewer number of Gauss-Newton iterations for all investigated noise levels. When the weights of EM data are increased, inversion results for  $k$  at high noise levels deteriorate. Moreover, the number of required Gauss-Newton iterations increases in comparison to uniform-weight joint inversion. In general, results indicate that the joint inversion approach yields more accurate  $k$  values at high noise levels in comparison to the inversion of time-lapse EM measurements. For all of the investigated cases,

inversion results for  $f$  appear to be very robust in the presence of noise. Despite this fact, a slight deterioration trend in the estimation of  $f$  is observed when the measurement noise level increases. For both inversion strategies, we reconstruct the conductivity domains sensed by the induction sonde at two logging times. This is accomplished by performing flow simulations using inverted model parameters. Figure 7 shows post-inversion conductivity domain reconstructions for log-test-log and time-lapse log strategies for each logging time, respectively. In the illustrated case, simultaneous inversion for  $k$  and  $f$  is carried out using dual-physics data contaminated with 7% white noise.

In the second numerical example (Case 2), we consider a vertically anisotropic formation with the following true model parameters: horizontal permeability,  $k_h = 100$  mD, vertical permeability,  $k_v = 20$  mD, and porosity,  $f = 0.25$ . All other parameters remain the same as in the previous case. We assume *a-priori* knowledge about  $k_h$  and stipulate the true value. Only joint inversion of uniformly weighted time-lapse magnetic field and pressure data at various levels of white noise is investigated for the simultaneous estimation of  $k_v$  and  $f$ . Initial guesses for model parameters are  $k_v = 50$  mD and  $f = 0.15$ . Inversion results are reported in Table 3 along with the required number of Gauss-Newton iterations for convergence. Inversion results indicate that the estimation of  $k_v$  remains robust up to 3% white noise level. Yet, at investigated noise levels higher than 3%, strong nonuniqueness renders the estimation of  $k_v$  inaccurate. Unlike the estimation of  $k_v$ , inverted  $f$  values are consistently accurate even at high noise levels. Extensive inversions conducted in this case indicate that the presence of multi-probe pressure data yields a significant improvement in the simultaneous estimation of  $k_v$  and  $f$ .

In the third numerical example (Case 3), we again consider a vertically anisotropic formation with the following true model parameters:  $k_h = 50$  mD,  $k_v = 5$  mD, and  $f = 0.18$ . All other information about the problem remains the same as that of Case 1. Joint inversion of uniformly weighted time-lapse magnetic field and pressure data at various levels of white noise is investigated for the simultaneous estimation of  $k_h$ ,  $k_v$ , and  $f$ . Initial guesses for model parameters are as follows:

$k_h = k_v = 100$  mD and  $f = 0.25$ . Inversion results are listed in Table 4. Inversions indicate that for up to 5% white noise level, the estimation of  $k_h$  remains robust. However, at noise levels higher than 5%, strong nonuniqueness renders the estimation of  $k_h$  inaccurate. The model parameter that is most sensitive to the deleterious effect of noise is  $k_v$ . The highest noise level that yields consistent inversion results for this parameter is 3%. Inverted  $f$  values remain consistently accurate even at high noise levels. Yet, a slight deterioration trend in the inversion results for  $f$  is observed when the noise level in the dual-physics data increases.

In the last numerical example (Case 4), we consider a dry-gas saturated formation made up of three anisotropic layers of various thicknesses shown in Fig. 3(b). Crossflow of fluids is allowed among the flow units. Formation rock and fluid properties, specific instrumental details, and scheduling of the above described measurement strategies are listed in Table 1. Layer-by-layer relative permeability and capillary pressure functions used for this numerical case are illustrated in Figs. 5(b) and 5(c). Simulated and averaged mud-filtrate invasion histories until the first logging time are shown in Fig. 6(c) for each flow-unit. Only log-test-log strategy is considered with the same measurement schedule as in the previous case except that the first logging time is assumed to be the 1<sup>st</sup> day of mud-filtrate invasion. During the formation test, the packer module is set across the lower-most layer and observation probes are located such that each probe is in contact with a separate layer. Joint inversion of uniformly weighted time-lapse magnetic field and pressure data at various levels of white noise is investigated for the simultaneous estimation of  $k_h$ ,  $k_v$ , and  $f$  for each layer. Actual and initial guess values for the model parameters, and inversion results are reported in Table 5. Inversion results clearly demonstrate the sensitivity of  $k_v$  in response to the effect of noise. Only at 1% noise level  $k_v$  values are accurately reconstructed. Estimation of  $k_h$  and  $f$  appear to be more robust in the presence of measurement noise in comparison to the estimation of  $k_v$ . High noise level negatively affects the estimation of model parameters of the most-permeable middle-layer. The quality of the estimation of model parameters for the top- and

bottom-most layers is relatively higher in comparison to that of the middle-layer.

## SUMMARY AND CONCLUSIONS

A dual-physics parametric inversion algorithm is developed and successfully employed to perform quantitative joint and independent interpretations of time-lapse EM induction and formation tester pressure transient measurements. The benefit of the inversion algorithm is the quantitative estimation of layer-by-layer horizontal and vertical absolute permeabilities, and porosities.

Inversion results indicate that the simultaneous use of dual-data sets effectively reduces the nonuniqueness and improves the stability of the optimization scheme. The positive impact of dual-physics data sets becomes significant when the measurements contain high levels of noise.

Parametric joint inversion of multi-probe pressure transient and time-lapse EM induction measurements can yield layer-by-layer horizontal and vertical near-wellbore permeabilities as well as porosities. In this case, the pressure transient test needs to be designed to ensure sensitivity of the transient data to the petrophysical parameters of the layers of interest. Model parameters that are most affected by the deleterious effect of noise are vertical permeabilities. Estimation of porosity is very robust to the effect of noise. Overall, porosity is the most accurately estimated model parameter.

Time-lapse EM induction measurements conducted across invaded beds can potentially yield significant information about the near-wellbore porosities and absolute permeabilities when interpreted within the framework of multiphase fluid flow. Pressure transient measurements contain first-order information about near-wellbore absolute permeabilities. Introduction of EM induction measurements to the inversion helps to further constrain absolute permeabilities. In effect, the main contribution of EM measurements is in providing first-order information about near-wellbore porosities, thereby, enabling the algorithm to simultaneously invert both near-wellbore permeabilities and porosities from noisy measurements.

## ACKNOWLEDGEMENTS

We would like to express our gratitude to Schlumberger for the funding of this work through a summer internship position provided to Faruk O. Alpak. Partial support of this work was provided by UT Austin's Research Consortium on Formation Evaluation, jointly sponsored by Baker

Atlas, Halliburton, Schlumberger, and Anadarko Petroleum Corporation. The authors also wish to thank Dr. Vladimir Druskin for valuable discussions and support throughout the course of the project.

## REFERENCES

Archie, G.E., 1942, The electrical resistivity log as an aid in determining some reservoir characteristics: *Petroleum Transactions of the AIME*, v. 146, p. 54-62.

Ayan, C., Hafez, H., Hurst, H., Kuchuk, F.J., O'Callaghan, A., Peffer, J., Pop, J., and Zeybek, M., 2001, Characterizing permeability with formation testers: *Oilfield Review*, Autumn issue, p. 1-23.

Aziz, K., and Settari, A., 1979, *Petroleum Reservoir Simulation*, Applied Science Publishers Ltd., London.

Blok, H., and Oristaglio, M., 1995, Wavefield imaging and inversion in electromagnetics and acoustics: Report number: Et/EM 1995-21, Laboratory of Electromagnetic Research, Department of Electrical Engineering Centre for Technical Geoscience, Delft University of Technology, Delft, The Netherlands.

Delshad, M., Pope, G.A., and Sepehrmoori, K., 1996, A compositional simulator for modeling surfactant enhanced aquifer remediation: *Journal of Contaminant Hydrology*, v. 23, p. 303-327.

Druskin, V., Knizhnerman, L., and Lee, P., 1999, New spectral Lanczos decomposition method for induction modeling in arbitrary 3D geometry: *Geophysics*, v. 64, n. 3, p. 701-706.

Eпов, M., Yeltsov, I., Kashevarov, A., Sobolev, A., and Ulyanov, V., 2002, Time evolution of the near borehole zone in sandstone reservoir through the time-lapse data of high-frequency electromagnetic logging, paper ZZ, in 43<sup>rd</sup> Annual Logging Symposium Transactions: Society of Professional Well Log Analysts, p. ZZ1-10.

Gill, P.E., Murray, W., and Wright, M.H., 1981, *Practical Optimization*, Academic Press, London.

Habashy, T.M., 2003, An inversion methodology using a weighted least-squares constrained minimization approach: Research note, Schlumberger-Doll Research, to be published.

Hunka, J.F., Barber, T.D., Rosthal, R.A., Minerbo, G.N., Head, E.A., Howard, A.Q., Hazen, G.A., and Chandler, R.N., 1990, A new resistivity measurement system for deep formation imaging and high-resolution formation evaluation, SPE 20559, in SPE Annual Technical Conference, Proceedings: Society of Petroleum Engineers, p. 295-307.

Moskow, S., Druskin, V., Habashy, T., Lee, P., and Davydycheva, S., 1999, A finite difference scheme for elliptic equations with rough coefficients using a Cartesian grid nonconforming to interfaces: *SIAM Journal on Numerical Analysis*, v. 36, n. 2, p. 442-464.

Pop, J., Badry, R., Morris, C., Wilkinson, D., Tottrup, P., and Jonas, J., 1993, Vertical interference testing with a wireline-conveyed straddle-packer tool, SPE 26481, in SPE Annual Technical Conference, Proceedings: Society of Petroleum Engineers, p. 665-680.

Ramakrishnan, T.S., and Wilkinson, D.J., 1997, Formation producibility and fractional flow curves from radial resistivity variation caused by drilling fluid invasion: *Physics of Fluids*, v. 9, n. 4, p. 833-844.

Ramakrishnan, T.S., and Wilkinson, D.J., 1999, Water-cut and fractional flow logs from array-induction measurements: *SPE Reservoir Evaluation & Engineering*, v. 2, n. 1, p. 85-94.

Semmelbeck, M.E., Dewan, J.T., and Holditch, S.A., 1995, Invasion-based method for estimating permeability from logs, SPE

30581, in SPE Annual Technical Conference, Proceedings: Society of Petroleum Engineers, p. 517-531.

Tobola, D.P., and Holditch, S.A., 1991, Determination of reservoir permeability from repeated induction logging: *SPE Formation Evaluation*, p. 20-26.

Torres-Verdín, C., and Habashy, T.M., 1994, Rapid 2.5-dimensional modeling and inversion via a new nonlinear scattering approximation: *Radio Science*, v. 29, n. 4, p. 1051-1079.

Wu, J., Torres-Verdín, C., Proett, M.A., Sepehrmoori, K., and Belanger, D., 2002, Inversion of multi-phase petrophysical properties using pumpout sampling data acquired with a wireline formation tester, SPE 77345, in SPE Annual Technical Conference, Proceedings: Society of Petroleum Engineers.

Yao, C.Y., and Holditch, S.A., 1996, Reservoir permeability estimation from time-lapse log data: *SPE Formation Evaluation*, p. 69-74.

Zeybek, M., Ramakrishnan, T.S., Al-Otaibi, S.S., Salamy, S.P., and Kuchuk, F.J., 2001, Estimating multiphase flow properties using pressure and flowline water-cut data from dual-packer formation tester interval tests and openhole array resistivity measurements, SPE 71568, in SPE Annual Technical Conference, Proceedings: Society of Petroleum Engineers.

Zhang, J.H., Hu, Q., and Liu, Z.H., 1999, Estimation of true formation resistivity and water saturation with a time-lapse induction logging method: *The Log Analyst*, v. 40, n. 2, p. 138-148.

## ABOUT THE AUTHORS

**Faruk O. Alpak** is a Research Assistant and a Ph.D. candidate in the Department of Petroleum Engineering at The University of Texas at Austin. His research interests include inverse problems, computational methods, reservoir simulation, numerical optimization, and electromagnetic wave propagation. He holds a M.Sc. degree in Petroleum Engineering from The University of Texas at Austin.

**Tarek M. Habashy** received a Ph.D. from MIT in 1983 in Electrical Engineering. During 1982-1983 he was a Research Associate in the Department of Electrical Engineering at MIT. Since September 1983, he has been with Schlumberger-Doll Research, and is now a Research Director of the Mathematics and Modeling Department. He is also a Scientific Advisor conducting research in electromagnetic logging tools, inverse scattering theory, and numerical analysis. He is the Editor of *Radio Science* and a member of the Editorial Boards of *Inverse Problems* and the *Journal of Electromagnetic Waves and Applications*. He is a Fellow of the Institute of Physics and IEEE.

**Carlos Torres-Verdín** received a Ph.D. in Engineering Geoscience from the University of California, Berkeley, in 1991. During 1991-1997 he held the position of Research Scientist with Schlumberger-Doll Research. From 1997-1999, he was Reservoir Specialist and Technology Champion with YPF (Buenos Aires, Argentina). Since 1999, he is an Assistant Professor with the Department of Petroleum and Geosystems Engineering of The University of Texas at Austin, where he conducts research in formation evaluation and integrated reservoir characterization. He has served as Guest Editor for *Radio Science*, and is currently a member of the Editorial Board of the *Journal of Electromagnetic Waves and Applications*, and an associate editor for *Petrophysics (SPWLA)*.

**Elizabeth B. Dussan V.** is a Scientific Advisor in the Real-Time Modeling and Inversion Theme at Schlumberger-Doll Research in Ridgefield, CT. Her degrees are in the field of fluid mechanics. Since joining Schlumberger in 1985 she has worked on different methods for determining permeability anisotropy and on the dynamics of filtrate invasion.

**TABLE 1:** Summary of geometrical, petrophysical, and fluid parameters employed in the construction of the reservoir models, where the hydrocarbon-saturated formation is invaded by the water-base mud. Note that we use the following encoding to distinguish data for various cases: (A) Cases 1, 2, and 3 [two-phase flow of oleic and aqueous phases, single-layer formation], and (B) Case 4 [two-phase flow of gaseous and aqueous phases, 3-layer formation]. Information about measurement schedules is also tabulated.

Variable	Units	Values
Mudcake permeability (A), (B)	[mD]	0.01, 0.03
Mudcake porosity (A), (B)	[fraction]	0.40, 0.60
Mud solid fraction (A), (B)	[fraction]	0.50, 0.20
Mudcake maximum thickness (A), (B)	[in]	1.00, 0.10
Formation rock compressibility (A), (B)	[psi <sup>-1</sup> ]	$5.00 \times 10^{-9}$ , $5.00 \times 10^{-9}$
Aqueous phase viscosity (mud-filtrate) (A), (B)	[cp]	1.274, 1.000
Aqueous phase density (mud-filtrate) (A), (B)	[lbm/cuft]	62.495, 74.040
Aqueous phase formation volume factor (mud-filtrate) (A), (B)	[rbbl/stb]	0.996, 1.000
Aqueous phase compressibility (mud-filtrate) (A), (B)	[psi <sup>-1</sup> ]	$2.55 \times 10^{-6}$ , $1.00 \times 10^{-6}$
Oleic phase viscosity (A)	[cp]	0.355
Oleic phase API density (A)	[°API]	42
Oleic phase density (A)	[lbm/cuft]	50.914
Oleic phase formation volume factor (A)	[rbbl/stb]	1.471
Oleic phase compressibility (A)	[psi <sup>-1</sup> ]	$1.904 \times 10^{-5}$
Fluid density contrast (A)	[lbm/cuft]	11.581
Viscosity ratio (water-to-oil) (A)	[dimensionless]	3.589
Initial water saturation (A)	[fraction]	0.30
Irreducible water saturation (A)	[fraction]	0.30
Residual oil saturation (A)	[fraction]	0.20
End-point relative permeability for aqueous phase (A)	[fraction]	0.25
End-point relative permeability for oleic phase (A)	[fraction]	0.80
Curvature parameter for aqueous phase relative permeability (A)	[dimensionless]	3.00
Curvature parameter for oleic phase relative permeability (A)	[dimensionless]	2.00
Gaseous phase viscosity [f(p) for T=const.] (B)	[cp]	0.01087@14.7 psia
Gaseous phase density [f(p) for T=const.] (B)	[lbm/cuft]	0.061@14.7 psia
Gaseous phase formation volume factor [f(p) for T=const.] (B)	[rbbl/Mscf]	139.203@14.7 psia
Initial water saturation (B)	[fraction]	Layer 1: 0.55, Layer 2: 0.50, Layer 3: 0.55
Irreducible water saturation (B)	[fraction]	Layer 1: 0.55, Layer 2: 0.50, Layer 3: 0.55
Residual gas saturation (B)	[fraction]	Layer 1: 0.03, Layer 2: 0.03, Layer 3: 0.03
End-point relative permeability for aqueous phase (B)	[fraction]	Layer 1: 0.12, Layer 2: 0.18, Layer 3: 0.12
End-point relative permeability for gaseous phase (B)	[fraction]	Layer 1: 0.50, Layer 2: 0.38, Layer 3: 0.50
Curvature parameter for aqueous phase relative permeability (B)	[dimensionless]	Layer 1: 3.00, Layer 2: 2.50, Layer 3: 3.00
Curvature parameter for gaseous phase relative permeability (B)	[dimensionless]	Layer 1: 2.00, Layer 2: 1.70, Layer 3: 2.00
Capillary pressure parameter for the gas-water system (B)	[psi × [mD] <sup>1/2</sup> ]	Layer 1: 30.00, Layer 2: 80.00, Layer 3: 50.00
Capillary pressure exponent for the gas-water system (B)	[dimensionless]	Layer 1: 2.50, Layer 2: 2.50, Layer 3: 2.50
Formation pressure (formation top is the reference depth) (A), (B)	[psia]	3000.00, 96.00
Mud hydrostatic pressure (A), (B)	[psia]	3600.00, 1153.00
Wellbore radius (A), (B)	[ft]	0.354, 0.350
Formation outer boundary location (A), (B)	[ft]	984.252, 984.252
Formation bed thickness (A)	[ft]	30.00
Formation bed thickness (B)	[ft]	Layer 1: 15.00, Layer 2: 6.00, Layer 3: 9.00
Relative depth of the top impermeable shoulder (A), (B)	[ft]	0.00, 0.00
Relative depth of the bottom impermeable shoulder (A), (B)	[ft]	30.00, 30.00
Pre rub-off mud-filtrate invasion duration (A)	[days]	Time-lapse log: 3, Log-test-log: 3
Post rub-off mud-filtrate invasion duration (A)	[days]	Time-lapse log: 7, Log-test-log: 0
Mudcake rub-off time (t <sub>first log</sub> ) (A)	[days]	Time-lapse log: 3, Log-test-log: 3
Second logging time (t <sub>second log</sub> ) (A)	[days]	Time-lapse log: 10, Log-test-log: 3.208
Formation horizontal permeability (A)	[mD]	Case 1: 100.00, Case 2: 100.00, Case 3: 50.00
Formation vertical permeability (A)	[mD]	Case 1: 100.00, Case 2: 20.00, Case 3: 5.00
Formation porosity (A)	[fraction]	Case 1: 0.25, Case 2: 0.25, Case 3: 0.18
Pre rub-off mud-filtrate invasion duration (B)	[days]	Log-test-log: 1
Post rub-off mud-filtrate invasion duration (B)	[days]	Log-test-log: 0
Mudcake rub-off time (t <sub>first log</sub> ) (B)	[days]	Log-test-log: 1
Second logging time (t <sub>second log</sub> ) (B)	[days]	Log-test-log: 1.208
Formation horizontal permeability (B)	[mD]	Layer 1: 6.83, Layer 2: 40.98, Layer 3: 14.33
Formation vertical permeability (B)	[mD]	Layer 1: 0.93, Layer 2: 4.53, Layer 3: 0.37
Formation porosity (B)	[fraction]	Layer 1: 0.139, Layer 2: 0.137, Layer 3: 0.125
Formation temperature (A), (B)	[°F]	220, 96
Formation brine salinity (A), (B)	[ppm]	120000, 200000
Mud-filtrate salinity (A), (B)	[ppm]	5000, 2000
a-constant in the Archie's equation (A), (B)	[dimensionless]	1.00, 1.00
m-cementation exponent in the Archie's equation (A), (B)	[dimensionless]	2.00, 2.00
n-water saturation exponent in the Archie's equation (A), (B)	[dimensionless]	2.00, 2.00
Mud conductivity (A), (B)	[mS/m]	2631.58, 387.60
Upper and lower shoulder bed conductivities (A), (B)	[mS/m]	1000.00, 400.0
Logging interval (A), (B)	[ft]	2.00, 2.00
<b>SPECIFIC INFORMATION FOR LOG-TEST-LOG SCHEDULE:</b>		
Drawdown duration (A), (B)	[min]	100.00, 100.0
Build-up duration (A), (B)	[min]	200.00, 200.0
Drawdown rate (A), (B)	[rbbl/d]	30.00, 1.50
3ft interval sealed by the dual-packer (DP) module (A), (B)	[ft]	[18.50, 21.50], [23.50, 26.50]
Location of the first observation probe (A), (B)	[ft]	5.00, 10.00
Location of the second observation probe (A), (B)	[ft]	13.00, 18.00
Location of the pressure measurement conducted by DP module (A), (B)	[ft]	20.00, 25.00

**TABLE 2:** Inversion results for formation permeability,  $k$ , and porosity,  $f$ , for Case 1, where,  $k_{true}=100$  mD &  $k_{initial\ guess}=40$  mD, and  $f_{true}=0.25$  &  $f_{initial\ guess}=0.12$ . Inversion results for  $k$  are reported in millidarcies [mD], and results for  $f$  are tabulated in volume fractions. For each inversion, the number of Gauss-Newton iterations necessary for convergence is also reported.

Inversion results for formation permeability, $k$			
Additive, Gaussian random noise level	Joint inversion Weight ratio: 1:1	Joint inversion Weight ratio: 1:3	Inversion of time-lapse EM data
0%	100.0008	100.4964	100.0119
1%	100.6252	101.6583	99.6669
3%	99.9802	103.6437	100.5998
5%	96.9803	103.7017	103.0344
6%	94.4246	101.2415	105.7765
7%	91.4730	98.0001	109.4154
8%	86.9841	85.1265	70.8595
Inversion results for formation porosity, $f$			
Additive, Gaussian random noise level	Joint inversion Weight ratio: 1:1	Joint inversion Weight ratio: 1:3	Inversion of time-lapse EM data
0%	0.2500000	0.2500001	0.2499997
1%	0.2499997	0.2500003	0.2499983
3%	0.2499995	0.2500001	0.2499959
5%	0.2499987	0.2500002	0.2499931
6%	0.2499980	0.2499996	0.2499919
7%	0.2499973	0.2499988	0.2499907
8%	0.2499967	0.2499966	0.2499825
Required number of Gauss-Newton iterations for convergence			
Additive, Gaussian random noise level	Joint inversion Weight ratio: 1:1	Joint inversion Weight ratio: 1:3	Inversion of time-lapse EM data
0%	6	9	4
1%	4	5	4
3%	4	4	5
5%	4	14	14
6%	4	11	14
7%	4	9	12
8%	5	40	34

**TABLE 3:** Joint inversion [weight ratio: 1:1] results for vertical permeability,  $k_v$ , and porosity,  $f$ , for Case 2. In this case, the value of horizontal permeability,  $k_h$ , is stipulated as *a-priori* information. Formation properties are:  $k_{h\ true}=100$  mD,  $k_{v\ true}=20$  mD, and  $f_{true}=0.25$ . The starting point for inversion is given by  $k_{v\ initial\ guess}=50$  mD &  $f_{initial\ guess}=0.15$ . For each inversion, the number of Gauss-Newton iterations necessary for convergence is also reported.

Additive, Gaussian random noise level	Stipulated horizontal permeability, $k_h$ [mD]	Inverted vertical permeability, $k_v$ [mD]	Inverted porosity, $f$ [fraction]	Number of Gauss-Newton iterations
0%	100.0000	19.9971	0.2500000	9
1%	100.0000	20.9036	0.2500003	23
3%	100.0000	23.2898	0.2500009	23
5%	100.0000	51.8645	0.2500093	6
8%	100.0000	50.4148	0.2500080	3

**TABLE 4:** Joint inversion [weight ratio: 1:1] results for horizontal and vertical permeability,  $k_h$  and  $k_v$ , and porosity,  $f$ , for Case 3, where, actual formation properties are:  $k_{h\ true}=50$  mD,  $k_{v\ true}=5$  mD, and  $f_{true}=0.18$ . The starting point for inversion is given by  $k_{h\ initial\ guess}=k_{v\ initial\ guess}=100$  mD. For each inversion, the number of Gauss-Newton iterations necessary for convergence is also reported.

Additive, Gaussian random noise level	Inverted horizontal permeability, $k_h$ [mD]	Inverted vertical permeability, $k_v$ [mD]	Inverted porosity, $f$ [fraction]	Number of Gauss-Newton iterations
0%	49.9997	5.0008	0.1800000	10
3%	49.5539	4.8851	0.1799160	11
5%	47.6620	4.8966	0.1797984	34
8%	40.7506	8.1786	0.1795293	28

**TABLE 5:** Inversion results for horizontal and vertical absolute permeabilities,  $k_h$  and  $k_v$ , and porosities,  $f$ , in the case of a 3-layer gas reservoir with its layers exhibiting vertical anisotropy [Case 4]. Actual formation properties are shown below. Initial guesses are as follows:  $k_{h,initial\ guess}=12.3884$  mD,  $k_{v,initial\ guess}=0.71$  mD (volume weighted arithmetic mean of horizontal and volume weighted harmonic mean of vertical permeabilities) and  $f_{initial\ guess}=0.18$ . For each inversion, the number of Gauss-Newton iterations necessary for convergence is also reported.

Inversion results for layer 1 [Joint inversion], where, $k_{h, true}=6.8300$ mD, $k_{v, true}=0.9300$ mD, and $f_{true}=0.1390000$				
Additive, Gaussian random noise level	$k_h$ [mD]	$k_v$ [mD]	$f$ [fraction]	Number of Gauss-Newton iterations
1%	6.8244	0.9379	0.1389886	17
3%	6.8319	0.7831	0.1389338	61
5%	6.8790	0.6175	0.1387820	15
8%	7.0049	0.3981	0.1384549	7
Inversion results for layer 2 [Joint inversion], where, $k_{h, true}=40.9783$ mD, $k_{v, true}=4.5300$ mD, and $f_{true}=0.1370000$				
Additive, Gaussian random noise level	$k_h$ [mD]	$k_v$ [mD]	$f$ [fraction]	Number of Gauss-Newton iterations
1%	44.6297	1.6917	0.1371555	17
3%	64.1831	22.0781	0.1376870	61
5%	92.4715	1.2876	0.1384260	15
8%	165.0117	1.7589	0.1396107	7
Inversion results for layer 3 [Joint inversion], where, $k_{h, true}=14.3311$ mD, $k_{v, true}=0.3700$ mD, and $f_{true}=0.1250000$				
Additive, Gaussian random noise level	$k_h$ [mD]	$k_v$ [mD]	$f$ [fraction]	Number of Gauss-Newton iterations
1%	14.3345	0.3653	0.1250063	17
3%	14.3278	0.4589	0.1247481	61
5%	14.3213	0.5017	0.1245766	15
8%	14.2363	0.8554	0.1238360	7

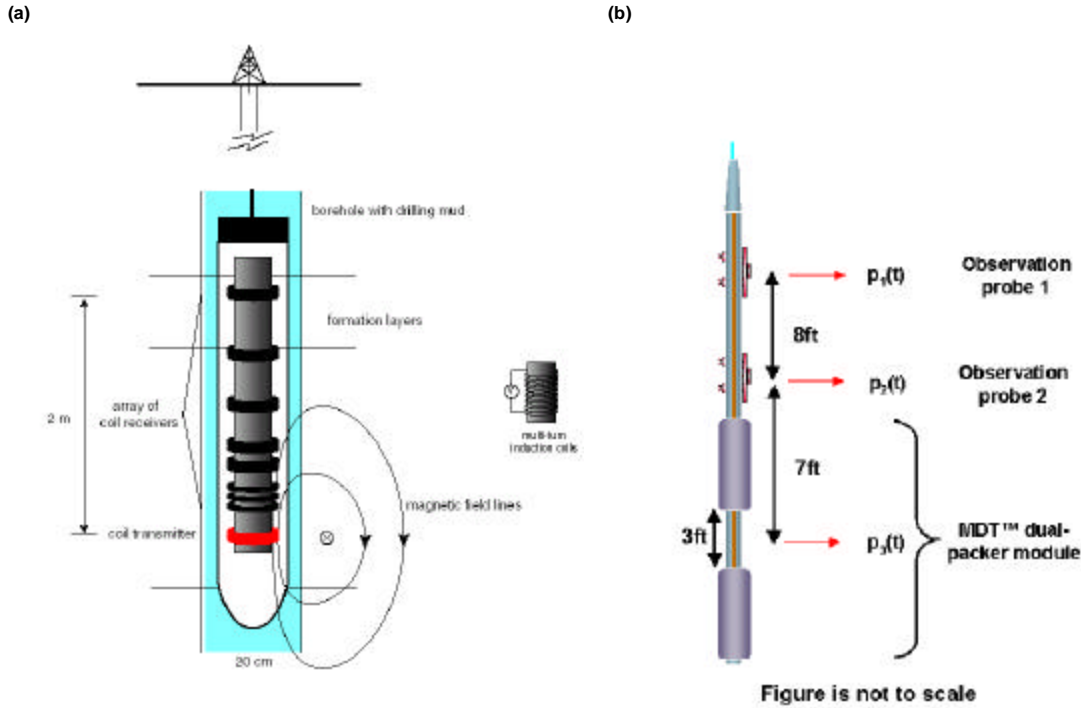


**FIG. 1:** (a) Induction logging with AIT: A multi-turn coil supporting a time-varying current generates a magnetic field that induces electrical currents in the formation. An array of receiver coils measures the magnetic field of the source and the secondary currents (Figure from Oristaglio and Blok, 1995). (b) Schematic of MDT multi-probe wireline tester packer/probe modules. The dual-packer module is combined with two vertical observation probes. Pressure transients are measured at three vertical locations in response to rate schedules imposed by a downhole pump. Fluid flow takes place through the packer open interval.

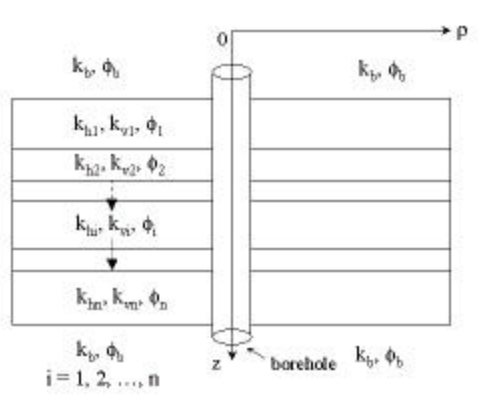


FIG. 2: Parameterization of the model domain in terms of horizontal geological layers. Model parameters are layer-by-layer horizontal and vertical absolute permeabilities, and porosities denoted by  $k_{hi}$ ,  $k_{vi}$ , and  $f$ , respectively.

(a)

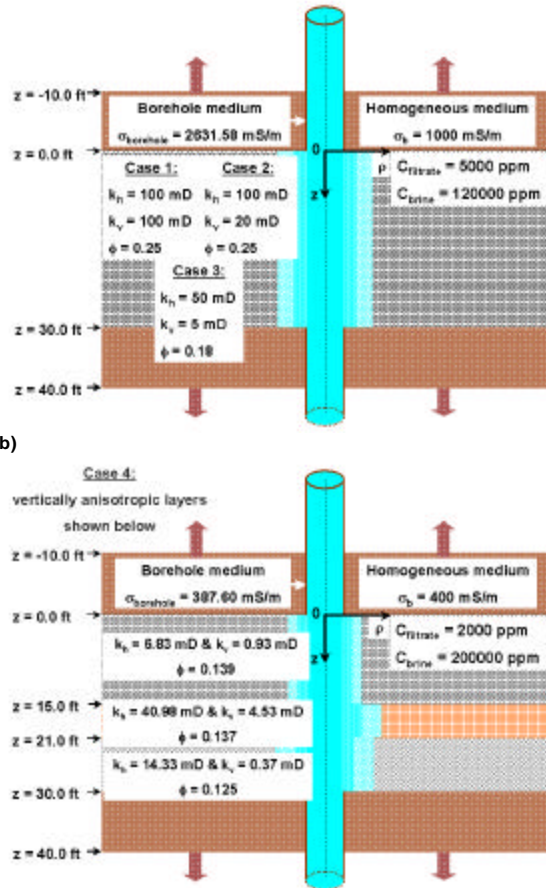


FIG. 3: Two-dimensional vertical cross-sections of the investigated formations of interest intersected by a vertical borehole. Example cases are considered for a 30ft-thick (a) single-layer, isotropic and anisotropic oil saturated formations, and (b) a 3layer, anisotropic dry-gas saturated formation. In both cases, the permeable zones of interest are subject to water-base mud-filtrate invasion. Presence of a conductivity contrast between invading and in-situ aqueous phases is assumed. Actual values of the model parameters for the investigated inversion cases and geoelectrical properties of the shoulder beds are shown above.

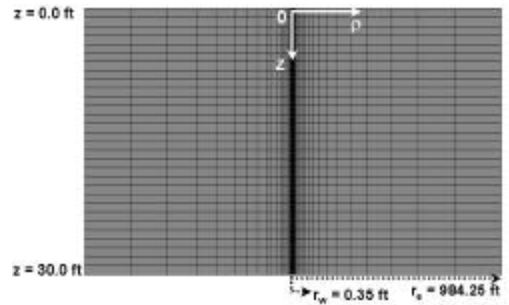
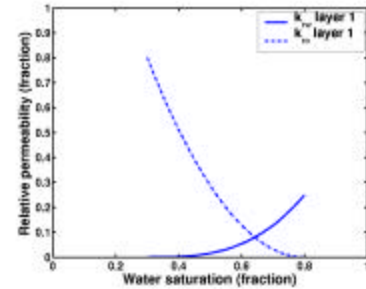
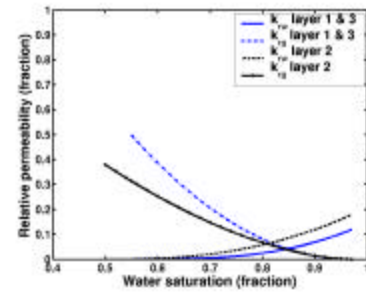


FIG. 4: Two-dimensional vertical cross-section of the finite-difference grid employed for fluid-flow simulations. The grid is of dimensions,  $r \times q \times z \cong 31 \times 6 \times 30$ , and is set up in a cylindrical coordinate system.

(a)



(b)



(c)

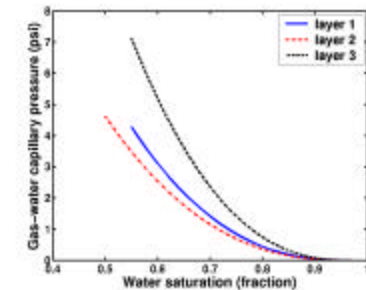


FIG. 5: (a) Relative permeability curves employed in two-phase fluid-flow simulations for Cases 1, 2, and 3. Capillary effects are assumed to be negligible. Layer-by-layer (b) relative permeability and (c) capillary pressure curves employed to model simultaneous flow of gaseous and aqueous phases for Case 4. In this case, each layer is treated as a separate saturation region with intrinsic saturation-dependent functions.

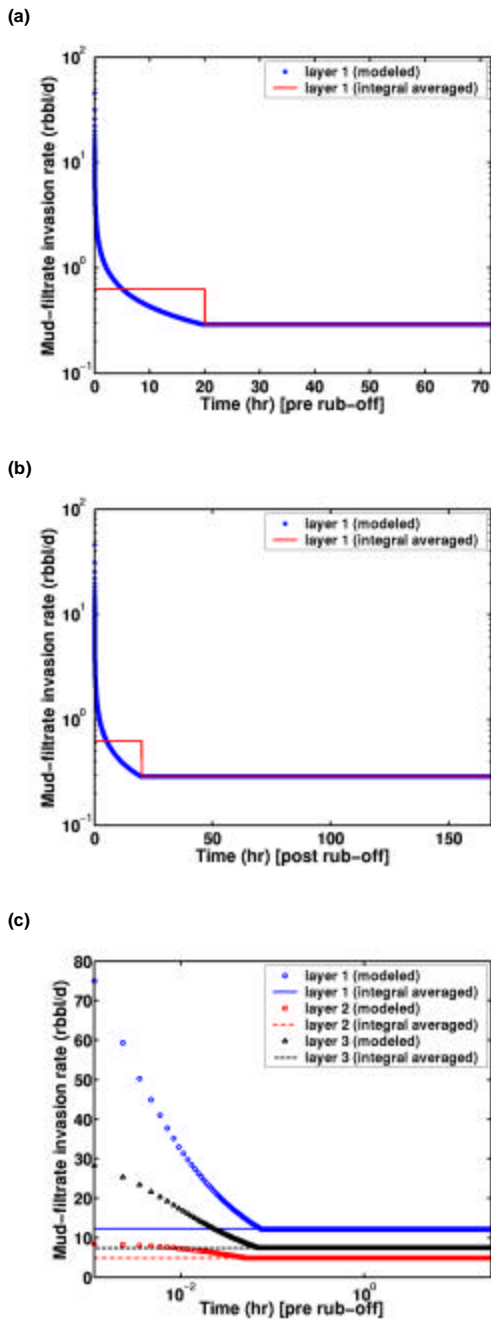
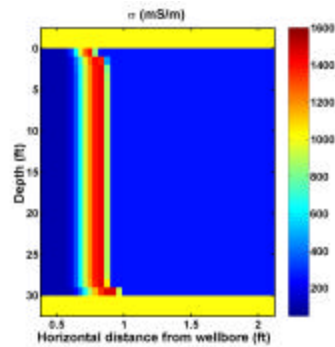
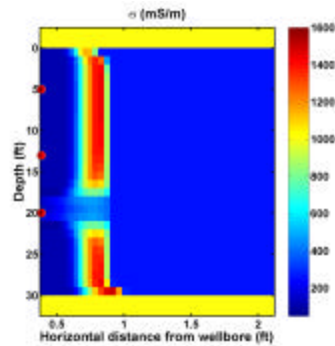


FIG. 6: Simulated (via using UTCHEM) and averaged (a) pre- and (b) post rub-off mud-filtrate invasion schedules for the single-layer formation [Cases 1, 2, and 3]. Simulation results are integral averaged via maintaining the total filtrate volumetric balance, and are expressed in terms of step-wise rate schedules for pre and post rub-off durations. (c) Simulated and integral averaged mud-filtrate invasion histories computed until the first logging time for each flow unit in case of the 3-layer formation [Case 4]. In this case, a single-step averaging scheme is used for each layer due to the short durations of the early-time transients.

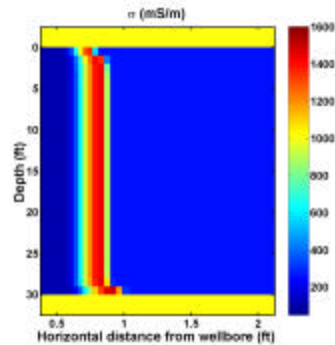
Log-test-log schedule:  $t_{log1} = 3$  days



Log-test-log schedule:  $t_{log2} = 3.208$  days



Time-lapse log schedule:  $t_{log1} = 3$  days



Time-lapse log schedule:  $t_{log2} = 10$  days

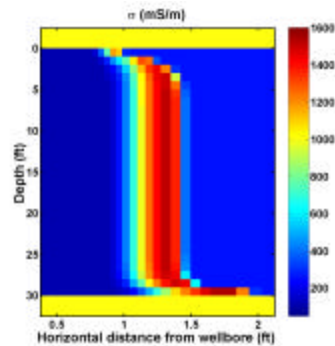


FIG. 7: Two-dimensional vertical cross-sections of the post-inversion conductivity domain reconstruction at two logging times for both log-test-log and time-lapse log schedules [Case 1]. In this case, simultaneous inversion for layer permeability and porosity is carried out using dual-physics data contaminated with 7% white noise.